

Hindrance in the fusion of $^{48}\text{Ca} + ^{48}\text{Ca}$ H. Esbensen,¹ C. L. Jiang,¹ and A. M. Stefanini²¹*Physics Division, Argonne National Laboratory, Argonne, Illinois 60439, USA*²*INFN, Laboratori Nazionali di Legnaro, I-35020 Legnaro (Padova), Italy*

(Received 7 October 2010; published 30 November 2010)

The coupled-channels technique is applied to analyze recent fusion data for $^{48}\text{Ca} + ^{48}\text{Ca}$. The calculations include the excitations of the low-lying 2^+ , 3^- , and 5^- states in projectile and target, and the influence of mutual excitations as well as the two-phonon quadrupole excitations is also investigated. The ion-ion potential is obtained by double-folding the nuclear densities of the reacting nuclei with the M3Y + repulsion effective interaction but a standard Woods-Saxon potential is also applied. The data exhibit a strong hindrance at low energy compared to calculations that are based on a standard Woods-Saxon potential but they can be reproduced quite well by applying the M3Y + repulsion potential with an adjusted radius of the nuclear density. The influence of the polarization of high-lying states on the extracted radius is discussed.

DOI: [10.1103/PhysRevC.82.054621](https://doi.org/10.1103/PhysRevC.82.054621)

PACS number(s): 24.10.Eq, 25.60.Pj, 25.70.-z

I. INTRODUCTION

Heavy-ion fusion reactions are sensitive probes of the nuclear surface of reacting nuclei. Roughly speaking, the height of the Coulomb barrier is determined by the radii and diffuseness of the densities, and the enhancement of fusion at subbarrier energies is governed by couplings to the excitation of low-lying surface modes [1]. This picture may not always succeed in reproducing the measured cross sections. In practical coupled-channels calculations it is often necessary to make adjustments, either in the structure input or in the ion-ion potential. The adjustments may reflect the influence of high-lying states or other reaction channels that are not treated explicitly in the calculations. Another complication is the hindrance of fusion, which occurs at low energies and very small cross sections [2]. The hindrance can be explained, for example, by using a shallow potential in the entrance channel [3] or by modeling the fusion dynamics for touching and overlapping nuclei [4].

In this work the coupled-channels technique is applied to analyze the fusion data for $^{48}\text{Ca} + ^{48}\text{Ca}$ that were recently measured down to very small cross sections below $1 \mu\text{b}$ [5]. An analysis of the data provides the opportunity to investigate whether the fusion hindrance, which is a well-established phenomenon in extreme subbarrier fusion reactions of medium-heavy systems with large negative Q values [2], also occurs in the fusion of calcium isotopes with near-zero Q values. An indication of a hindrance in the fusion of $^{48}\text{Ca} + ^{48}\text{Ca}$ has already been observed [5] because the low-energy data could only be reproduced by coupled-channels calculations that employ a very large diffuseness of the ion-ion potential. However, the hindrance observed there was not strong enough to show an S factor maximum in the energy region of the measurement.

The ion-ion potential and the nuclear couplings that will be used are derived as in previous work [3] from the double-folding of the densities of the reacting nuclei and the M3Y + repulsion effective interaction. Since the low-lying structure of ^{48}Ca is fairly well established and the influence

of transfer reactions is always suppressed for symmetric systems, it is expected that this simple picture of fusion just described would apply to the fusion of $^{48}\text{Ca} + ^{48}\text{Ca}$. On the other hand, it is well known that the excitation and/or polarization of high-lying states that are included explicitly in the coupled-channels calculations can lead to a negative energy shift of the calculated fusion cross sections [6]. This is effectively equivalent to increasing the radii of the reacting nuclei. The radius that is extracted by optimizing the fit to the fusion data can therefore be too large because it can be contaminated by the polarization of states which are not included explicitly in the calculations. It is of interest to see how the extracted radius depends on the model space of excited states that are included in the calculations, and how well it compares to the expected matter radius of ^{48}Ca .

The study of the fusion of different calcium isotopes started more than twenty years ago with the measurements by Aljuwair *et al.* [7] but the cross sections were only measured down to about 1 mb . The most challenging theoretical issue at that time was to explain the fusion of $^{40}\text{Ca} + ^{48}\text{Ca}$, which appeared to be strongly enhanced by couplings to transfer reactions, in particular to those with positive Q values [8,9]. A strong motivation for reviving the study of the fusion of calcium isotopes is that, in addition to $^{48}\text{Ca} + ^{48}\text{Ca}$ [5], the fusion of $^{40}\text{Ca} + ^{48}\text{Ca}$ has also recently been measured down to the $1 \mu\text{b}$ level [10], and a new measurement for $^{40}\text{Ca} + ^{40}\text{Ca}$ is underway [11]. In order to be able to focus on and isolate the effect of transfer on the fusion of the asymmetric $^{40}\text{Ca} + ^{48}\text{Ca}$ system, it is necessary first to develop a good description of the fusion of the two symmetric systems, and the present work is a step in that direction.

The nuclear structure properties of ^{48}Ca are discussed in the next section and Sec. III describes the construction of the ion-ion potential. The coupled-channels technique is summarized in Sec. IV together with an analysis of the data that is based on Woods-Saxon potentials. The analysis based on the M3Y + repulsion potential is presented in Sec. V. Finally, the conclusions are given in Sec. VI.

TABLE I. Nuclear structure input for ^{48}Ca . Values marked with * are from Ref. [12]. The $B(E\lambda)$ values are from Ref. [14]. They are consistent with the Coulomb excitation parameters $(\beta R)_C/\sqrt{4\pi}$, except for the 3^- state where Ref. [12] uses a larger value, $B(E3) = 6.8$ W.u. The lower part of the table shows the three transitions that determine the effective two-phonon quadrupole state. Its excitation energy and couplings to the 2_1^+ state are shown in the last line.

I^π	E_x (MeV)	$B(E\lambda)$ (W.u.)	$\frac{(\beta R)_C}{\sqrt{4\pi}}$ (fm)	$\frac{(\beta R)_N}{\sqrt{4\pi}}$ (fm)
2_1^+	3.832	1.71(9)	0.126*	0.190*
3^-	4.507	5.0(8)	0.250*	0.190*
5^-	5.146		0.049*	0.038*
$0_2^+ \rightarrow 2_1^+$	4.283	10.1(6)	[0.098]	
$4^+ \rightarrow 2_1^+$	4.503	0.261(6)	[0.025]	
$2_2^+ \rightarrow 2_1^+$	5.311	9(9)	[0.111]	
Eff 2PH	4.849	4.7(29)	0.15	0.15

II. NUCLEAR STRUCTURE INPUT

The nuclear structure input to the coupled-channels calculations is shown in Table I. The elastic channel and the one-phonon excitations of the low-lying 2^+ , 3^- , and 5^- states in projectile and target results in a total of seven channels. The coupling strengths for the excitation of these states are taken from Ref. [12] where they were calibrated by analyzing the elastic and inelastic scattering of ^{16}O on calcium isotopes [13]. It should be noted that the Coulomb and nuclear coupling strengths, expressed in Table I by the values of $\beta R/\sqrt{4\pi}$, are different. The Coulomb couplings are in most cases consistent with the currently adopted electromagnetic transition probabilities or B values [14] that are quoted in the third column of Table I.

Also shown in Table I are the 0^+ , 2^+ , and 4^+ members of two-phonon quadrupole excitation. The adopted $B(E2)$ values [14] shown in the third column of the lower part of Table I can be combined into an effective two-phonon excitation. For example, the effective $B(E2)$ value for the two- to one-phonon transition is given by the sum,

$$B(E2, 2\text{ph} \rightarrow 1\text{ph}) = \sum_{I=0,2,4} \langle 2020|I0 \rangle^2 B(E2, I \rightarrow 2), \quad (1)$$

and the two-phonon excitation energy is obtained as the weighted average of the individual two-phonon excitations energies [15]. The parameters obtained for the effective two-phonon quadrupole excitation are shown in the last line of Table I. Including the effective two-phonon quadrupole excitations in the coupled-channels calculations, in addition to the seven channels just mentioned, leads to a total of nine channels. Unfortunately, nothing is known about the two-phonon excitations of the 3^- and 5^- states so they will be ignored.

To get a feeling for the influence of higher-order excitations on the calculated fusion cross sections one can also include all of the 15 mutual excitations channels that are generated from the 6 one-phonon excitations presented in Table I. Together

with the basic 9 channels already mentioned, that sums up to a total of 24 channels. This will be referred to as the full calculation and the results will be compared to the fusion data and to calculations that include the 9 channels just described, as well as the no-coupling limit, in which case there is only a single channel.

III. THE ION-ION POTENTIAL

The parameters of the Woods-Saxon (WS) potentials that will be used in this work,

$$U_{\text{WS}}(r) = \frac{-V_0}{1 + \exp[(r - R_0)/a]}, \quad (2)$$

are those proposed in Ref. [16], Eqs. (III.2.40–45). The parameters for the system $^{48}\text{Ca} + ^{48}\text{Ca}$ are $a = 0.662$ fm for the diffuseness and $V_0 = 64.10$ MeV for the depth of the potential. We refer to this potential as the “standard” WS potential because its diffuseness is consistent with the analysis of elastic scattering data [16]. The radius R_0 , on the other hand, will be treated as a free parameter and it will be adjusted to optimize the fit to the data in the coupled-channels calculations that are discussed in the next section.

There is an interesting point concerning the isospin dependence of the nuclear potential proposed in Ref. [16]. It enters through the average nuclear surface tension γ of the reacting nuclei,

$$\gamma = 0.95 \left(1 - 1.8 \frac{N_a - Z_a}{A_a} \frac{N_b - Z_b}{A_b} \right) \text{ MeV fm}^{-2}, \quad (3)$$

according to Ref. [16], Eq. (III.2.30). The correction factor in Eq. (3), which depends on neutron excess, is equal to one in reactions that involve ^{40}Ca . In the case of $^{48}\text{Ca} + ^{48}\text{Ca}$, the correction factor reduces the surface tension by 5%; this correction is included in the value of the depth parameter V_0 used here.

The M3Y + repulsion potential is calculated using the double-folding technique described in Ref. [3]. It is based on the Reid parametrization of the M3Y effective nucleon-nucleon interaction [17]. The spherical nuclear densities are parametrized by

$$\rho(r) = \frac{1}{2} \frac{\rho_0 \exp(R/a)}{\cosh(r/a) + \cosh(R/a)}, \quad (4)$$

where R and a are the radius and diffuseness parameters, respectively, and ρ_0 is a normalization constant. It is seen that the density, Eq. (4), approaches the Fermi function density $\rho_0/\{1 + \exp[(r - R)/a]\}$ for $R/a \gg 1$. The parametrization given by Eq. (4) is used here because it has some very useful analytic properties as discussed in the Appendix of Ref. [18]. For example, the Fourier transform has an analytic form, which simplifies the calculation of the double-folding potential in Fourier space from the expression [3],

$$U(r) = \frac{1}{2\pi^2} \int k^2 dk \rho(k) \rho(k) v_{nn}(k) j_0(kr), \quad (5)$$

where $v_{nn}(k)$ is the Fourier transform of the effective nucleon-nucleon interaction, and $j_0(x) = \sin(x)/x$ is a spherical Bessel function. Another advantage of the parametrization given by

Eq. (4) is that the mean-square radius is given by the simple expression

$$\langle r^2 \rangle = \frac{3}{5} \left[R^2 + \frac{7}{3} (a\pi)^2 \right]. \quad (6)$$

The repulsive part of the M3Y + repulsion potential is determined by two parameters, namely, the strength v_r of the contact effective interaction,

$$v_{nn}^{\text{rep}}(\mathbf{r}) = v_r \delta(\mathbf{r}), \quad (7)$$

that generates it, and the diffuseness a_r of the densities that are applied in the double-folding calculation [3]. The radius parameter R of the densities, on the other hand, is kept the same as in the calculation of the direct and the exchange parts of the M3Y double-folding potential. The diffuseness of the density that is used in calculating the direct and the exchange parts of the M3Y potential is kept fixed with the value $a = 0.54$ fm.

The two parameters a_r and v_r of the repulsive part of the potential are constrained so that total nuclear potential energy, $U_N(r)$, for completely overlapping nuclei is consistent with the equation of state. That leads to the relation [3]

$$U_N(r=0) \approx \frac{A_p}{9} K, \quad (8)$$

where A_p is the mass number of the smaller nucleus and K is the nuclear incompressibility. For $^{48}\text{Ca} + ^{48}\text{Ca}$ the value $K = 223.7$ MeV predicted by the Thomas-Fermi model of Myers and Świątecki [19] will be used. Thus there are essentially only two free parameters of the M3Y + repulsion interaction, namely, the radius R and the diffuseness parameter a_r . They will be adjusted to optimize the fit to the fusion data. The strength v_r of the repulsive interaction, on the other hand, is constrained for given values of R and a_r by the nuclear incompressibility according to Eq. (8).

Some of the entrance channel potentials that are used in this work are illustrated in Fig. 1. The height of the Coulomb barrier is essentially the same for all four potentials but the thickness of the barrier is very different. The (blue) dashed curve is the entrance channel potential for the Woods-Saxon potential. It has the minimum pocket energy $V_{\text{min}} = 23.09$ MeV and the height of the Coulomb barrier is $V_{\text{CB}} = 51.63$ MeV. The latter potential was determined by optimizing the fit to the fusion data with center-of-mass energy larger than 50 MeV. This energy cut was chosen because the fusion hindrance phenomenon sets in below 50 MeV, as we shall see in the next section.

The upper two curves in Fig. 1 are the M3Y + repulsion entrance channel potentials that are obtained in Sec. V. They were determined by optimizing the fit to the fusion data in coupled-channels calculations that include the 24 channels described in Sec. II. There are two solutions, the M3Y + rep-1 and M3Y + rep-2 potentials, both of which are discussed in detail in Sec. V. These potentials are shallower than the standard Woods-Saxon potential, which is a characteristic feature of the M3Y + repulsion potentials that have been extracted from fusion data [3].

Finally, the entrance channel potential for the pure M3Y(+exchange) potential is also shown. It is unrealistic because it is deeper than the ground-state energy of the

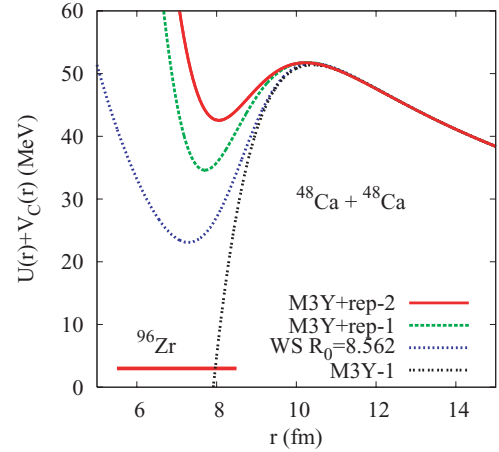


FIG. 1. (Color online) Entrance channel potentials for $^{48}\text{Ca} + ^{48}\text{Ca}$ obtained from the Woods-Saxon (WS, with $R_0 = 8.562$ fm) and the pure M3Y (M3Y-1) potentials. The two upper curves are the shallow M3Y + repulsion potentials determined in Sec. V. The energy of the ground state of the compound nucleus ^{96}Zr is also indicated.

compound nucleus ^{96}Zr , which is indicated by the thick horizontal line.

IV. COUPLED-CHANNELS CALCULATIONS

The coupled-channels calculations are performed in the rotating-frame approximation, and the fusion cross sections are determined by imposing ingoing-wave boundary conditions at the position of the minimum of the pocket in the entrance potential. This procedure is commonly used and is described, for example, in Refs. [3,20]. In the present work no imaginary potential will be applied. The fusion cross section will therefore vanish when the center-of-mass energies are lower than the minimum energy of the pocket in the entrance channel potential.

The nuclear potential enters the coupled equations both directly by determining the entrance channel potential and indirectly by determining the nuclear couplings to first and second order in the deformation amplitudes through the first and second derivatives of the nuclear potential (see Ref. [20] for details). There are, in principle, couplings of even higher order and to higher-lying states [21] but they will be ignored in the present study, partly because they are poorly known and partly because they are not expected to play a large role in the fusion of the not-so-heavy system $^{48}\text{Ca} + ^{48}\text{Ca}$. This expectation is based on the experience gained in Ref. [15]. However, the polarization of high-lying states [6] that are not included in the calculations could distort the analysis.

The fusion data for $^{48}\text{Ca} + ^{48}\text{Ca}$ [5] are compared in Fig. 2 to two coupled-channels calculations that are based on standard Woods-Saxon potentials [16] with the diffuseness $a = 0.662$ fm and depth $V_0 = 64.10$ MeV. All 24 channels described in Sec. II were included in the calculations. It is seen that the data are hindered at low energies and the energy dependence is much steeper than predicted by the calculations. The dashed curve in Fig. 2 is the best fit to all data points; it

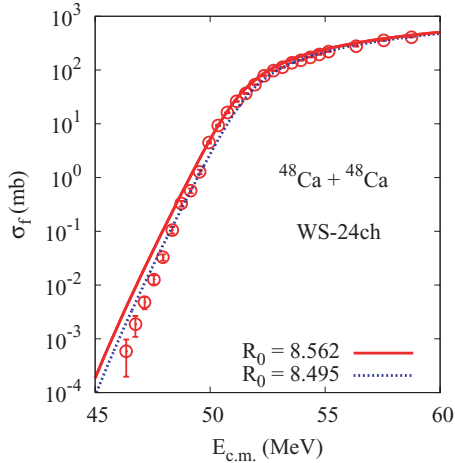


FIG. 2. (Color online) Fusion cross sections for $^{48}\text{Ca} + ^{48}\text{Ca}$. The error bars reflect the statistical uncertainties. The curves are coupled-channels calculations with 24 channels that use Woods-Saxon (WS) potentials with two different radii.

is achieved with radius $R_0 = 8.495$ fm but the fit is very poor with an average χ^2 per data point of $\chi^2/N = 7.9$, including the statistical uncertainties and a systematic error of 7%.

The solid curve in Fig. 2 is based on the slightly larger radius, $R_0 = 8.562$ fm. It provides a better account of the data near and above the the Coulomb barrier, as discussed in the following. The associated entrance channel potential is the (blue) dashed curve shown in Fig. 1.

The behavior of the hindrance in the fusion of $^{48}\text{Ca} + ^{48}\text{Ca}$ is illustrated in Fig. 3 in terms of the ratio of the measured and calculated fusion cross sections. It is seen that the ratio with respect to the best fit to the data (the solid diamonds) has a strong peak near 50 MeV, slightly below the Coulomb barrier, which is at $V_{\text{CB}} \approx 52$ MeV. The ratio drops quickly at energies below 50 MeV. This is attributed to the fusion hindrance phenomenon. In fact, the steep falloff with decreasing energy observed in the comparison to standard coupled-channels

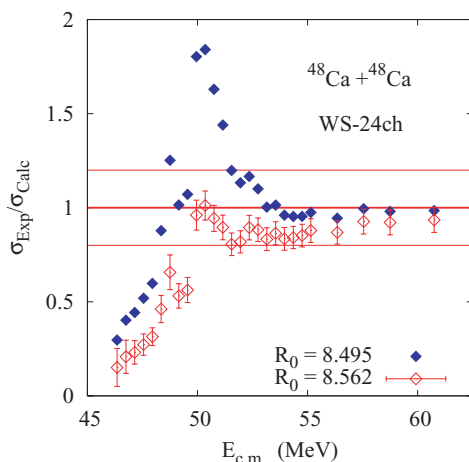


FIG. 3. (Color online) Ratios of the measured and calculated cross sections shown in Fig. 2. The error bars on the open diamonds were determined by the statistical uncertainties and a 7% systematic error.

calculations was the signature that was first used to identify the fusion hindrance [22]. Later it was shown that the hindrance is often so strong that the S factor for fusion develops a maximum at very low energies. Moreover, it was realized that an S factor maximum together with the energy E_S of the maximum is a good quantitative way to characterize the fusion hindrance phenomenon [23].

Since the fusion hindrance occurs at low energies one may exclude the low-energy region and focus on reproducing the data at higher energies. The result of this approach is shown in Fig. 2 by the solid curve, which is based on a slightly larger radius, $R_0 = 8.562$ fm. The larger radius implies larger cross sections below the Coulomb barrier but that gives a better description of the excitation function in the barrier region. The radius of the Woods-Saxon potential was therefore chosen so that the ratio of the measured and calculated cross sections essentially is a constant above 50 MeV. This is illustrated by the open diamonds in Fig. 3. It is seen that the fusion hindrance sets in very strongly below 50 MeV, where the ratio falls off very steeply with decreasing energy.

V. ANALYSIS BASED ON THE M3Y + REPULSION POTENTIAL

The parameters of the M3Y + repulsion potential that provides the best fit to the data were determined using an improved calibration procedure. For a given nuclear radius parameter R of ^{48}Ca and a given diffuseness a_r of the density used in calculating the repulsive part of the potential, the strength of the repulsive term v_r was adjusted so that the incompressibility $K = 223.7$ MeV was achieved in Eq. (8). Having determined the nuclear potential, we performed coupled-channels calculations and the average χ^2 per data point, χ^2/N , was calculated from the statistical uncertainties and a systematic error of 7%.

This procedure was repeated with different values of the radius R for a fixed diffuseness parameter a_r until a minimum χ^2/N was found. The whole process was repeated for a new value of a_r . The results of this process are illustrated in Fig. 4, where χ^2/N , minimized with respect to the radius R , is plotted as a function of the diffuseness parameter a_r . The dashed curve is the result of calculations that include the 9 channels and the solid curve is the result obtained with all 24 channels described in Sec. II.

The fusion data of Ref. [5] are compared in Fig. 5 to various calculations. The solid curve is the result of coupled-channels calculations associated with the deepest minimum in Fig. 4, which has a χ^2 per data point of 1.66. The upper (blue) dashed curve shows the cross sections obtained in similar calculations using the Woods-Saxon potential with the radius $R_0 = 8.562$ fm. All 24 channels described in Sec. II were included in both sets of calculations. The only difference between the two calculations is the choice of the nuclear potential, and it is seen that the shallow M3Y + repulsion potential labeled M3Y + rep-2 is a much better choice.

The lowest dashed curve in Fig. 5 is the cross section obtained in the no-coupling limit (i.e., with only one channel) using the same M3Y + repulsion potential that was used to produce the solid curve. By comparing the two curves, it is

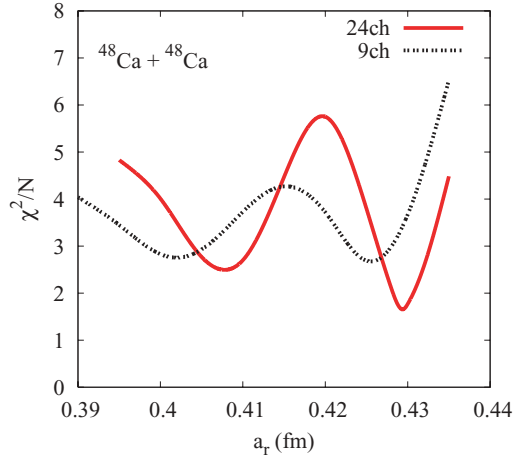


FIG. 4. (Color online) Results of the χ^2 analysis of the $^{48}\text{Ca} + ^{48}\text{Ca}$ fusion data [5]. χ^2/N , minimized with respect to the radius R , is shown as a function of the diffuseness parameter a_r . The solid curve (24 ch) is for calculations that include 24 channels; the dashed curve (9 ch) is for 9 channels.

seen that the effect of the couplings to the 24 channels is equivalent to shifting the no-coupling limit almost 1 MeV to lower energies.

A. Details of the analysis

The minima of the curves shown in Fig. 4 define the stable solutions of the χ^2 analysis of the fusion data since they are minima with respect to variations in both a_r and R . There are two local minima for each set of calculations, and the parameters of the M3Y + repulsion interactions that determine them are given in Table II. It is seen the two solutions obtained with nine coupled channels have almost the same χ^2/N . It is not clear what causes the existence of two solutions. The main

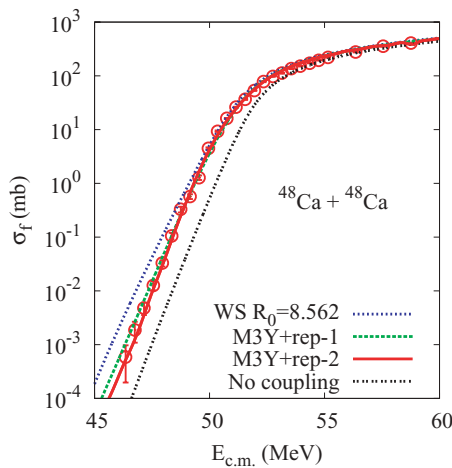


FIG. 5. (Color online) Fusion cross sections for $^{48}\text{Ca} + ^{48}\text{Ca}$. The upper two curves are coupled-channels calculations with 24 channels that are based on the Woods-Saxon (WS) and the M3Y + repulsion (M3Y + rep-1 and M3Y + rep-2) potentials discussed in the text. The lowest dashed curve is the no-coupling limit based on the same M3Y + repulsion potential.

TABLE II. Parameters of the M3Y + repulsion potential associated with the χ^2 minima in Fig. 4. Results are shown for coupled-channels calculations that include 9 and 24 channels, respectively. The last three columns show the minimum of the pocket, V_{\min} , the height of the Coulomb barrier, V_{CB} , and the χ^2 value per data point.

Number of channels	R (fm)	a_r (fm)	v_r (MeV fm ³)	V_{\min} (MeV)	V_{CB} (MeV)	χ^2/N
9	3.775	0.4025	480.1	33.58	51.67	2.76
9	3.810	0.4250	504.2	41.66	51.60	2.69
24	3.745	0.4070	481.8	34.61	51.77	2.52
24	3.798	0.4295	505.6	42.55	51.73	1.66

difference between them is that the energy of the pocket in the entrance channel potential, V_{\min} , is about 8 MeV deeper in the solution with the smaller radius R .

Of the two solutions obtained with 24 channels, the one with the larger radius gives a much better fit to the data with $\chi^2/N = 1.66$ and the associated potential will be referred to as the M3Y + rep-2 potential. The potential for the solution with the smaller radius is called the M3Y + rep-1 potential. The two entrance channel potentials are illustrated in Fig. 1. An important question is whether the parameters of the stable solutions are realistic, or whether some of them can be ruled out as being unrealistic. One parameter of particular interest is the radius, which is examined next.

The rms radii obtained for the stable solutions are shown in the fourth column of Table III. They can be compared to the estimated experimental rms matter radius of ^{48}Ca shown in the last line of the table. The estimate was based on the rms radius of the proton distribution, which was obtained from the measured rms charge radius [24], and the experimental rms radius of the neutron distribution [25]. The neutron radius is uncertain and several values exist in the literature. The

TABLE III. The radius R of ^{48}Ca extracted from the analysis of the fusion data (cf. Table II). The rms radii are compared to the measured rms charge [24], proton [24], and neutron [25] radii. The latter two have been combined into the rms matter radius shown in the last line. The quoted matter radius ([3.75] fm) was derived by inserting the rms matter radius and the diffuseness $a = 0.54$ fm into Eq. (6).

Reference	Number of channels	R (fm)	$\langle r^2 \rangle^{1/2}$ (fm)
	9	3.755	3.547
	9	3.810	3.569
M3Y + rep-1	24	3.745	3.528
M3Y + rep-2	24	3.798	3.562
charge [24]			3.474(1)
protons			3.387(1)
neutrons [25]			3.63(5)
matter		[3.75]	3.53(3)

TABLE IV. χ^2/N values (column 3) obtained in calculations that use the M3Y + rep-2 potential and include 1, 9, or 24 channels. The energy shift ΔE of the calculations that optimizes the fit to the data and the associated χ^2/N values are shown in the last two columns.

R (fm)	Channels	χ^2/N	ΔE (MeV)	χ^2/N
3.798	1	33.3	-0.80	4.65
3.798	9	4.28	-0.12	2.71
3.798	24	1.66	0.0	1.66

experimental value chosen here was obtained from an analysis of elastic proton scattering data at 800 MeV [25] and is in fairly good agreement with most of the theoretical predictions shown in Table I of Ref. [26].

The estimated rms matter radius quoted in the last line of Table III is in perfect agreement with the rms radius associated with the M3Y + rep-1 solution. The rms radius for the M3Y + rep-2 solution is larger but it is still consistent with the experimental estimate within the 1σ uncertainty. A possible explanation for the larger radius could be the influence of the polarization of high-lying states not included in the calculations (see the following).

It is also encouraging that the extracted values of a_r shown in Table II are similar to those determined in the analysis of the fusion data for $^{64}\text{Ni} + ^{64}\text{Ni}$ ($a_r = 0.403$ fm [3]), $^{16}\text{O} + ^{16}\text{O}$ ($a_r = 0.41$ fm [27]), and $^{48}\text{Ca} + ^{96}\text{Zr}$ ($a_r = 0.40$ fm [28]). It is noted that in the previous works the densities (including the radius) were kept fixed and only the value of a_r was adjusted in each case to improve the fit to the data.

B. Polarization effects

The polarization effect discussed in Sec. I is illustrated in Table IV. The table shows that, for the M3Y + rep-2 potential, one needs to shift the one-channel calculation by $\Delta E = -0.80$ MeV and the nine-channel calculation by -0.12 MeV in order to optimize the fit to the data. The negative energy shifts are equivalent to using a larger radius of the reacting nuclei. For example, the required energy shift of -0.12 MeV for the calculations with nine channels can be simulated by increasing the radius of ^{48}Ca by only 0.02 fm.

The required energy shift ΔE shown in Table IV for the calculation with 24 channels is zero simply because the radius R was already adjusted in this case to optimize the fit to the data. The issue of whether the calculations have converged with respect to the excitation and polarization of high-lying states is a difficult one to address. It is possible that the polarization of other high-lying states, which have not been considered here, could play a role and explain part of the 0.05 fm difference between the radius of the M3Y + rep-2 solution and the estimated experimental matter radius (see Table III).

C. S factor representation

A good way to illustrate the behavior of the fusion cross section σ_f at low energies is to plot the S factor for fusion,

$$S = E_{\text{c.m.}} \sigma_f \exp(\eta - \eta_0), \quad (9)$$

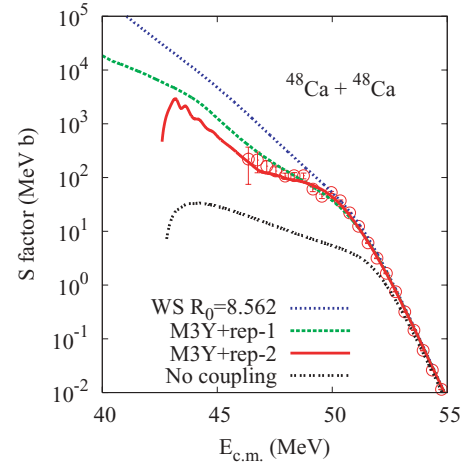


FIG. 6. (Color online) S factors for the fusion cross sections shown in Fig. 5. Also shown is the S factor obtained in calculations with the M3Y + rep-1 potential. All calculations include 24 channels, except the no-coupling limit, which has only 1 channel.

where $\eta = Z_1 Z_2 e^2 / (\hbar v)$ is the Sommerfeld parameter and η_0 is that value of η at a fixed reference energy E_0 . The S factors for the fusion cross sections shown in Fig. 5 are illustrated in Fig. 6 using the (arbitrary) reference energy $E_0 = 52$ MeV. Also shown is the result obtained with the M3Y + rep-1 potential and 24 coupled channels.

The coupled-channels calculations for the Woods-Saxon potential produce an S factor in Fig. 6 that keeps increasing with decreasing energy. The S factors obtained with the two M3Y + repulsion potentials and 24 coupled channels are lower. The S factor for the best fit to the data (the solid curve, obtained with the M3Y + rep-2 potential) has a maximum at $E_s = 43.2$ MeV. The cross section associated with the latter maximum is very small, about 0.3 nb. The S factor for the calculation based on the M3Y + rep-1 potential has a maximum at $E_s = 35.4$ MeV, which is outside the depicted energy range.

It would be very interesting to know whether the predicted S factor maximum near $E_s = 43.2$ MeV can be confirmed by experiments, but to measure a cross section of only 0.3 nb would be a serious challenge.

D. Logarithmic derivative

The logarithmic derivative of the energy-weighted cross sections,

$$L(E_{\text{c.m.}}) = \frac{d}{dE_{\text{c.m.}}} \ln(E_{\text{c.m.}} \sigma_f), \quad (10)$$

is illustrated in Fig. 7. The logarithmic derivatives derived from the data and from the coupled-channels calculation based on the M3Y + rep-2 potential (the solid curve) are seen to be in very good agreement. Similar results were obtained in Ref. [5] in coupled-channels calculations that used a Woods-Saxon potential with the large diffuseness $a = 0.9$ fm. Thus it appears that a large diffuseness of the Woods-Saxon has an effect that is similar to that of the shallow M3Y + repulsion potential, at least in the low-energy region discussed here.

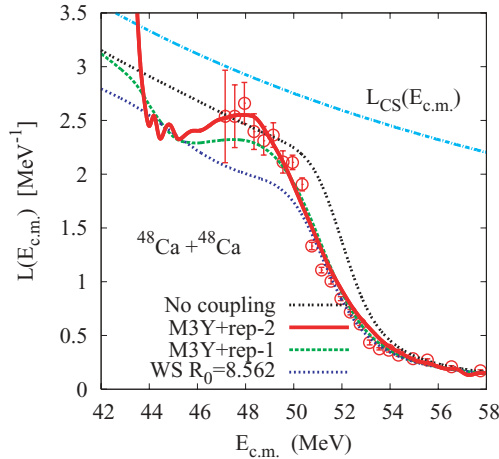


FIG. 7. (Color online) The logarithmic derivative of the energy-weighted cross sections shown in Fig. 5. Also shown is the result of coupled-channels calculations based on the M3Y + rep-1 potential. The top curve is the constant S factor limit, $L_{CS}(E_{c.m.})$.

The similarity of the M3Y + repulsion and a Woods-Saxon potential was recently pointed out in Ref. [29]. It was shown that the M3Y + repulsion potential can be reproduced accurately in the barrier region by a Woods-Saxon potential with large diffuseness. However, a nuclear potential with a large diffuseness is inconsistent with many measurements of elastic and quasielastic scattering. For example, a recent systematic study of quasielastic scattering of nuclei showed that a realistic diffuseness in the range of 0.64 to 0.69 fm is indeed required [30].

It is very interesting to point out that the low-energy behavior of the experimental logarithmic derivative shown in Fig. 7 is different from the behavior observed in other systems, in particular in medium-heavy systems [2], where the logarithmic derivative usually increases linearly with decreasing energy and intersects with the logarithmic derivative for constant S factor [23],

$$L_{CS}(E_{c.m.}) = \pi \eta / E_{c.m.} \quad (11)$$

However, there are other systems that exhibit a deviant behavior at low energies. For example, the logarithmic derivative for the fusion of $^{36}\text{S} + ^{48}\text{Ca}$ [31] also becomes rather flat at low energies and it seems unlikely that it will intersect with the constant S factor limit. In fact, the S factor for the fusion of

$^{36}\text{S} + ^{48}\text{Ca}$ increases slowly and linearly in a logarithmic plot with decreasing energy (see Fig. 3 of Ref. [31]).

Another interesting point is that the solid curve in Fig. 7 exhibits a maximum near 48 MeV before it rises steeply below 44 MeV. It intersects with the constant S factor limit at $E_s = 43.2$ MeV, where the associated S factor in Fig. 6 develops a maximum.

VI. CONCLUSIONS

The fusion data for $^{48}\text{Ca} + ^{48}\text{Ca}$ have been analyzed using the coupled-channels technique and different ion-ion potentials. The analysis based on a standard Woods-Saxon potential clearly showed that the data are strongly hindered at low energies. By employing and adjusting the M3Y + repulsion double-folding potential it was possible to achieve an excellent description of the data.

The best fit to the data was achieved with a nuclear radius of ^{48}Ca that is slightly larger than but still consistent with the matter radius of ^{48}Ca . The latter radius was determined from the measured rms charge radius and the rms neutron radius extracted from an analysis of elastic proton scattering data. The fact that the extracted radius is slightly larger than the matter radius may be caused by the polarization of high-lying states that are not included in the coupled-channels calculations.

The entrance channel potential for the best fit to the data has a rather shallow pocket, consistent with the findings of previous analyses of fusion data for medium-heavy systems. The M3Y + repulsion potential model is therefore also referred to as the shallow potential model, in contrast to models based on the standard Woods-Saxon potentials, which have relatively deep pockets in the entrance channel potential.

The S factor for the fusion of $^{48}\text{Ca} + ^{48}\text{Ca}$ does not show a maximum within the energy range of the experiment. However, it is predicted to develop a maximum 3 MeV lower in energy, which is nearly the same as the energy value obtained from the extrapolation method in Ref. [10]. The cross section associated with the maximum S factor is very small (≈ 0.3 nb) and is a serious challenge to the experimental technology.

ACKNOWLEDGMENTS

One of the authors (H.E.) acknowledges discussions with Ş. Mişicu about double-folding potentials. This work was supported by the US Department of Energy, Office of Nuclear Physics, Contract No. DE-AC02-06CH11357.

- [1] A. B. Balantekin and N. Takigawa, *Rev. Mod. Phys.* **70**, 77 (1998).
- [2] C. L. Jiang, B. B. Back, H. Esbensen, R. V. F. Janssens, and K. E. Rehm, *Phys. Rev. C* **73**, 014613 (2006).
- [3] Ş. Mişicu and H. Esbensen, *Phys. Rev. C* **75**, 034606 (2007).
- [4] T. Ichikawa, K. Hagino, and A. Iwamoto, *Phys. Rev. C* **75**, 064612 (2007); *Phys. Rev. Lett.* **103**, 202701 (2009).
- [5] A. M. Stefanini *et al.*, *Phys. Lett. B* **679**, 95 (2009).
- [6] K. Hagino, N. Takigawa, and A. B. Balantekin, *Phys. Rev. C* **56**, 2104 (1997).
- [7] H. A. Aljuwair *et al.*, *Phys. Rev. C* **30**, 1223 (1984).
- [8] S. Landowne, C. H. Dasso, R. A. Broglia, and G. Pollarolo, *Phys. Rev. C* **31**, 1047 (1985).
- [9] H. Esbensen, S. H. Fricke, and S. Landowne, *Phys. Rev. C* **40**, 2046 (1989).
- [10] C. L. Jiang *et al.*, *Phys. Rev. C* **82**, 041601(R) (2010).
- [11] A. M. Stefanini (private communications, 2010).
- [12] H. Esbensen and F. Videback, *Phys. Rev. C* **40**, 126 (1989).
- [13] K. E. Rehm, W. Henning, J. R. Erskine, D. G. Kovar, M. H. Macfarlane, S. C. Pieper, and M. Rhoades-Brown, *Phys. Rev. C* **25**, 1915 (1982).

- [14] Evaluated Nuclear Structure Data Files, National Nuclear Data Center, Brookhaven National Laboratory, [<http://www.nndc.bnl.gov/>].
- [15] H. Esbensen, *Phys. Rev. C* **72**, 054607 (2005).
- [16] R. A. Broglia and A. Winther, *Heavy-ion Reactions*, Frontiers in Physics Lecture Notes Series, Vol. 84 (Addison-Wesley, Redwood City, CA, 1991).
- [17] G. Bertsch, J. Borysowicz, H. McManus, and W. G. Love, *Nucl. Phys. A* **284**, 399 (1977).
- [18] H. Esbensen and Ş. Mişicu, *Phys. Rev. C* **76**, 054609 (2007).
- [19] W. D. Myers and W. J. Świątecki, *Phys. Rev. C* **57**, 3020 (1998).
- [20] H. Esbensen, *Phys. Rev. C* **68**, 034604 (2003).
- [21] K. Hagino, N. Takigawa, M. Dasgupta, D. J. Hinde, and J. R. Leigh, *Phys. Rev. C* **55**, 276 (1997).
- [22] C. L. Jiang *et al.*, *Phys. Rev. Lett.* **89**, 052701 (2002).
- [23] C. L. Jiang, H. Esbensen, B. B. Back, R. V. F. Janssens, and K. E. Rehm, *Phys. Rev. C* **69**, 014604 (2004).
- [24] I. Angeli, *At. Data Nucl. Data Tables* **87**, 185 (2004).
- [25] L. Ray, *Phys. Rev. C* **19**, 1855 (1979).
- [26] J. Dobaczewski, W. Nazarewicz, and T. R. Werner, *Z. Phys. A* **354**, 27 (1996).
- [27] H. Esbensen, *Phys. Rev. C* **77**, 054608 (2008).
- [28] H. Esbensen and C. L. Jiang, *Phys. Rev. C* **79**, 064619 (2009).
- [29] O. N. Godsi and V. Zanganeh, *Nucl. Phys. A* **846**, 40 (2010).
- [30] C. J. Lin, H. M. Jia, H. Q. Zhang, F. Yang, X. X. Xu, F. Jia, Z. H. Liu, and K. Hagino, *Phys. Rev. C* **79**, 064603 (2009).
- [31] A. M. Stefanini *et al.*, *Phys. Rev. C* **78**, 044607 (2008).